Wind filtering evidence of mesospheric short-period gravity waves revealed from all-sky images at King Sejong Station (62°S, 59°W)

H. Kam[1,2], J.-H. Kim[2*], Y. H. Kim[1], I.-S. Song[2], B.-G. Song[2], T. Nakamura[3,4], Y. Tomikawa[3,4], M. Kogure[5], M. K. Ejiri[3,4], S. Perwitasari[6], M. Tsutsumi[3,4]

(Hosik Kam[1,2], Jeong-Han Kim[2*], Yong Ha Kim[1], In-Sun Song[2], Byeong-Gwon Song[2], Takuji Nakamura[3,4], Yoshihiro Tomikawa[3,4], Masaru Kogure[5], Mitsumu K. Ejiri[3,4], Septi Perwitasari[6], Masaki Tsutsumi[3,4])

[1]Department of Astronomy, Space Science and Geology, Chungnam National University, Daejeon, South Korea

[2]Division of Polar Climate Sciences, Korea Polar Research Institute, Incheon, South Korea

[3]National Institute of Polar Research, Tokyo, Japan

[4]Department of Polar Science, SOKENDAI (The Graduate University for Advanced Studies) Tokyo, Japan

[5]Faculty of Sciences, Kyushu University, Fukuoka, Japan

[6]National Institute of Information and Communications Technology, Tokyo, Japan

Corresponding author: Jeong-Han Kim (jhkim@kopri.re.kr)

Key Points:

- M-transform analysis of all-sky OH airglow images observed for 5 years objectively characterizes mesospheric short-period GW spectra.
- Monthly mean diagrams of wave directions and wind blockings clearly reveal wind filtering effects on most of slow speed waves.
- However, eastward waves in winter and southeast waves in Oct. are not blocked by stratospheric winds, suggesting their origins in the mesosphere.

Abstract

We analyzed OH airglow images observed from an all-sky camera at King Sejong Station, Antarctica for the period of 2012–2016. Using M-transform method, 2D-power spectra of short period waves (< 1 hr) were obtained from 107 image sequences. The power spectral densities evidently show that the mesospheric wave activity is the strongest during winter. We also constructed climatological wind blocking diagrams using horizontal winds obtained from MERRA-2 for the altitudes of z= 10–64 km, and from KSS meteor radar data for z = 80–90 km. The wind blocking diagrams are negatively matched with the dominant propagating directions of the observed slow speed waves (< 30 m/s), providing the graphical evidence of wind filtering effects. However, there are significant eastward waves in winter and strong south-eastward waves in spring that are not blocked by the stratospheric winds. We speculate that these waves may be generated from the upper stratosphere or mesosphere.

1 Introduction

Dynamics in the mesosphere and lower thermosphere (MLT) region is substantially influenced by the energy and momentum transport from the lower atmosphere through vertically propagating atmospheric gravity waves (GWs). In the MLT region, momentum deposition due to GW breaking or dissipation in mid- to high-latitude regions induces acceleration and deceleration of the zonal wind in each hemisphere and thus generates the pole-to-pole residual circulations across two hemispheres which makes cold summer and warm winter mesopause at high latitudes (Lindzen, 1981; Fritts and Alexander, 2003; Becker, 2012). In general, GWs are ubiquitously generated due to orography, deep convection, wind shear, baroclinic instability, cold front, jet flow, and by other mechanisms (Fritts and Alexander, 2003).

Various observational and modeling studies have revealed that GW activities are particularly intense over Southern Andes and Antarctic Peninsula called ‘GW hot spot’ region (Ern et al., 2004; Alexander and Teitelbaum, 2007; Baumgaertner and McDonald, 2007; Hindley et al., 2015). This region is well poised for generating GWs and even secondary GWs since it is in suitable orography and near the polar vortex (Preusse et al., 2002; Sato et al., 2009; de Wit et al., 2017; Becker and Vadas, 2018; Liu et al., 2019). Furthermore, intense

wave activities have been reported in the mesosphere over King Sejong Station (KSS, 62°S, 58°W) located in the "GW hot spot" using meteor radar wind data (Lee et al., 2013).

The vertical propagation of GWs depends on the relationship between horizontal phase velocity of GWs and background horizontal wind. When horizontal phase velocity vectors of GWs become close to local horizontal wind vectors as GWs propagate vertically, they are absorbed in the mean flow or reflected back, and thus filtered out, as being called 'critical-level filtering' (Fritts and Alexander, 2003). This critical-level filtering is essential in understanding spectral properties of GWs observed in the MLT region.

Spectral properties of small-scale GWs in the MLT such as their wavelength, phase speed, and propagating direction can be directly observed in airglow layers using optical imagers. Taylor et al. (1993) investigated properties of mesospheric short-period GWs observed from airglow images and found that the propagation properties can be accounted for by critical level filtering by background winds using a blocking diagram. The blocking diagram illustrates spectral properties of upward propagating GWs that would not be detected at airglow altitudes. However, the interpretation of observed propagation properties with the wind blocking diagram requires accurate and objective analysis of observed airglow images. Analysis of airglow images has often been carried out through subjective image processes that may vary depending on personal preferences of researchers. To overcome the disadvantage of the subjective methods, Matsuda et al. (2014) developed a new analysis method (hereafter, M-transform) to obtain power spectra as a function of the horizontal phase speed and azimuth angle from a sequence of normalized airglow intensity images. Using the M-transform, Matsuda et al. (2017) derived successfully characteristics of mesospheric GWs from Antarctic Gravity Wave Instrument Network (ANGWIN) imagers at Syowa (69°S, 40°E), Halley (76°S, 27°W), Davis (69°S, 78°E), and McMurdo (78°S, 167°E).

In this study, we investigate wind filtering of GWs in airglow images observed at King Sejong Station (62°S, 58°W, KSS) for 5 years (2012-2016) by applying the M-transform method. Kam et al. (2017) reported statistical distributions of individual wave structures in the airglow images using the traditional subjective analysis method. The use of M-transform method enables to obtain spectral properties from fainter wave signals than before. We derived predominant propagating directions and magnitudes of short period GWs. We also constructed wind blocking diagrams from the reanalysis wind data of middle atmosphere and meteor radar wind data measured at KSS. By comparing propagating directions of observed GWs with wind blocking diagrams, we were able to show graphically

wind filtering effects on vertically propagating GWs and found that some of observed waves were generated above the stratosphere.

2 Data and Analysis

2.1 Airglow images observed with an all-sky camera

An all-sky camera (ASC) at KSS has been operated by Korea Polar Research Institute (KOPRI) since 2008. The KSS ASC consists of a fish-eye-lens with 180° field of view, telecentric lens of two Plano-convex lens, two narrow- and one wide-band interference filters, multi-wavelength filter wheel (with OH Meinel bands, OI 557.7 nm, and OI 630.0 nm), and a 1024 × 1024 CCD with 2 × 2 binning. Detailed specifications of the instrument and basic image pre-processing methods are described in Kam et al. (2017). In this study, we analyzed OH Meinel bands images which were observed with a band filter of 720 nm - 910 nm. The OH images are regarded to reflect the OH airglow layer at an altitude of 87 km, and thus have a spatial resolution of 1.17 km/pixel. The OH images were obtained with an exposure time of 20 sec at sampling interval of 328 sec. This study utilized OH images observed from 2012 to 2016 since the instrument was upgraded in 2012. Because OH images are in higher quality than other filter images and the OH layer is at the lowest altitude, we chose to analyze only OH images to investigate wind filtering effect of middle atmosphere on vertical propagation of GWs.

2.2 Utilizing M-transform

To investigate the morphology of wave activities, we utilized the M-transform as the new method of spectral analysis for ASC image sequence data set (hereafter; image-time window). The M-transform introduced by Matsuda et al. (2014) results in spectral powers on horizontal phase speed domain. The M-transform has an advantage of facilitating uniform products: 3-D distributions of power spectrum density as a function of frequency, zonal wavenumber, and meridional wavenumber. The 3-D spectrum was integrated in the frequency domain, resulting in a 2-D phase velocity distribution. According to Perwitasari et al. (2018), the M-transform can be utilized as a user-friendly function that only requires image sequence data (normalized intensity

as $(I - \bar{I})/\bar{I}$ $(= I'/\bar{I})$; I is the pixel intensity observed from airglow and $\bar{I}$ is the temporal averaged intensity for image-time window), with wave parameters (range for horizontal wavelength, wave period, and phase speed) and the sampling information (time interval, image size, and resolution). In this study, we chose the ranges for horizontal wavelengths of 10 - 100 km, wave periods of 15 - 60 min, and phase speeds of 0 - 150 m/s. To select the image-time window of clear sky from marginally cloudy images, we set the criteria of efficient grids on the unwarped (pre-processed) images as the region of interest in each image-time window for the purpose of avoiding clouds and the galactic contamination due to the wide band nature of the OH filter. The criteria are as follows: the grid size for analyzing image should be larger than 150×150 km^2 on the OH airglow layer, the duration time for clear sky is over 1 hour on successive images, and the grid size is fixed in single image-time window (each window has a different grid size). Conventionally, GW studies with ASC images have been proceeded by analyzing specific images containing visible wave structures. However, in this study, we analyzed all the images of clear sky in accordance with our criteria. During the 5 years, the ratio of analysis time to the total ASC operated time is merely about 7% because of bad weather condition at KSS. The total number of image-time windows for the M-transform analysis is 107 windows. As an example, Figures 1a and 1b show an $I'_{OH}/\overline{I_{OH}}$ image observed on the 30 June, 2014 and its 3-D power spectral density (hereafter; PSD) on the phase velocity domain from M-transform, respectively. Predominant wave crests seem to align NW-SE in Figure 1a, and the maximum power spectra on the horizontal phase velocity domain stand out in the third quadrant (indicating SW propagation in accordance of the visible crest alignment) with speed range of 20-50 m/s in Figure 1b.

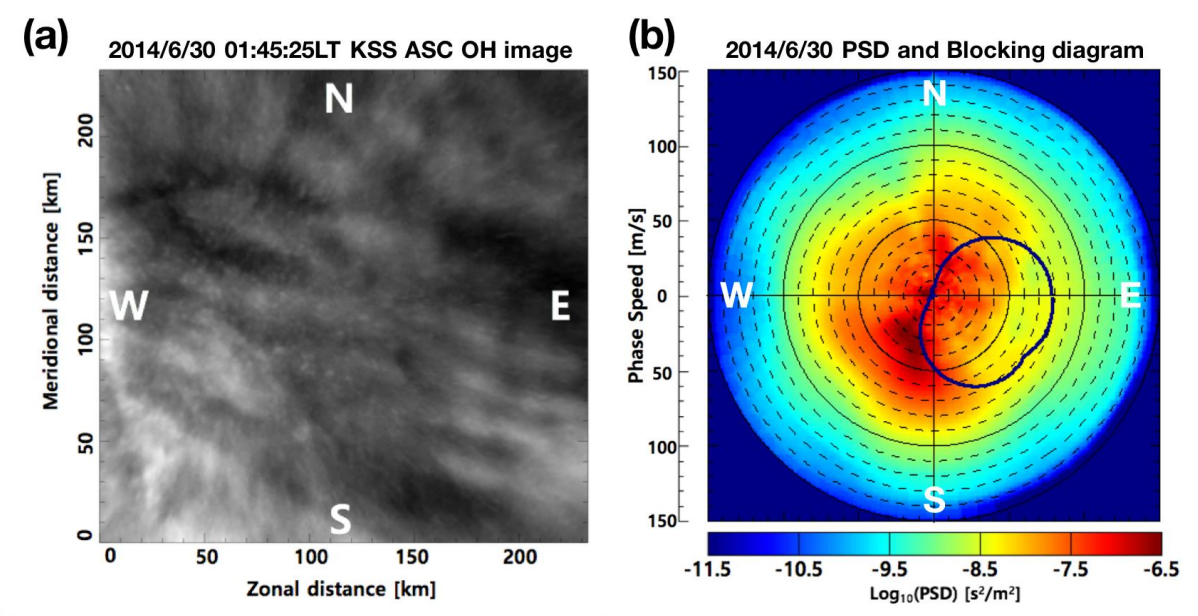

Figure 1. Example of OH airglow images for (a) $\boldsymbol{I'_{OH}/\overline{I_{OH}}}$ from one image at 01:45:25LT 30 June, 2014 and (b) power spectra on phase velocity domain of corresponding image-time window (23:43:17LT 29 June ~ 04:46:55LT 30 June, 2014) and the over-plotted navy line represents a wind blocking diagram.

149

150 2.3 Wind data from KSS meteor radar and MERRA-2

151 To construct wind blocking diagrams, stratospheric winds and mesospheric
152 winds were obtained from the Modern-Era Retrospective analysis for Research and
153 Applications, version-2 (MERRA-2) (Gelaro et al., 2017) and the meteor radar (MR)
154 located at KSS, respectively. Since March 2007, KSS MR has been operating in the
155 all-sky interferometer mode with a peak power of 12 kW (8 kW before 2012) using a
156 center frequency 33.2 MHz, and the configurations of KSS MR are detailed in Lee et
157 al. (2013). The KSS MR provides mesospheric horizontal winds in the altitude range
158 of 80 – 100 km with height and time resolutions of 2 km and 1 hour, respectively. The
159 MERRA-2 database is a global atmospheric reanalysis dataset produced by the NASA
160 Global Modeling and Assimilation Office. The MERRA-2 provides data 4-times a
161 day (00:00, 06:00, 12:00, and 18:00 UTC) with horizontal spacing of $1.25° \times 1.25°$
162 and 42 vertical pressure levels corresponding to the range of 0 - 64 km altitude. The
163 horizontal winds of MERRA-2 were selected around the location of KSS within $\pm 5°$
164 in longitude and latitude, and were daily averaged for the day of specific image-time
165 window.

166 We adopted a method of Taylor et al. (1993) to construct wind blocking
167 diagrams by combining the horizontal wind profiles of MERRA-2 at altitudes of 10-
168 64 km and MR winds at 80-90 km. The lower boundary (i.e., the altitude where GWs
169 are emitted) was set at 10 km because tropospheric winds are not strong enough and
170 GWs can be generated near the tropopause. The upper boundary of 90 km was chosen
171 by considering a full-width at half maximum of OH airglow layer of 8 km (Baker and
172 Stair, 1988). There is a data gap between the wind measured altitude of MERRA-2
173 and MR over KSS, from 64 km to 80 km. An example of wind blocking diagram is
174 over-plotted in Figure 1b with a navy line in polar coordinate (r, θ) where r and θ
175 represent the maximum blocking wind in unit of m/s and the azimuthal angle,
176 respectively.

177

3 Results and Discussions

3.1 Seasonal characteristics of short period GWs

The sum of power spectral density (total PSD) of each image-time window, as shown in Figure 1b, can represent the short period GW activity. In order to examine a seasonal variation of GW activities, we computed monthly averaged total PSD over the observed years, as presented in Figure 2a. The maximum wave activity occurs in Austral winter (June), as noted in the previous study (Kam et al., 2017). The standard deviation of the monthly mean total PSD is also maximized in June, implying high variability of the wave activities. Previous observations over Antarctic Peninsula have reported the intense wave activities during winter in the mesosphere (Espy et al., 2006), the stratosphere (Jiang et al., 2003; Baumgaertner and McDonald, 2007; Sato et al., 2012; Hoffmann et al., 2013, 2017) and the thermosphere (Park et al., 2014). The coincidence of the seasonal characteristics from the stratosphere to thermosphere suggests that observed short period waves in OH airglow images be upward propagating GWs generated from typical sources in the troposphere. However, the tropospheric GWs and other waves, including planetary waves and tides, may cause the observed wave activities in the upper atmosphere, not just by direct propagation but by secondary wave generation after their break-up on the way. Recently, using a high-resolution global circulation model, Becker and Vadas (2018) suggested that secondary GWs are well generated during winter from body force of breaking primary waves in the stratosphere and lower mesosphere around 60°S.

Before to investigate propagation directions of observed waves in terms of wind filtering, we examined the phase speed distribution from the M-transform analysis, as presented in Figure 2b. The phase speed represents the apparent horizontal propagation speed of waves in the sequence of observed images. The observed waves have dominantly slow speeds, as can be seen in Figure 2b. In order to investigate the seasonal variation of propagating directions, we divided the observed waves into three groups according to their phase speeds: slow waves for 0 – 30 m/s, medium waves for 30 – 50 m/s and fast waves for 50 – 100 m/s. The slow, medium and fast waves are 52%, 29%, and 19 % of all the observed waves.

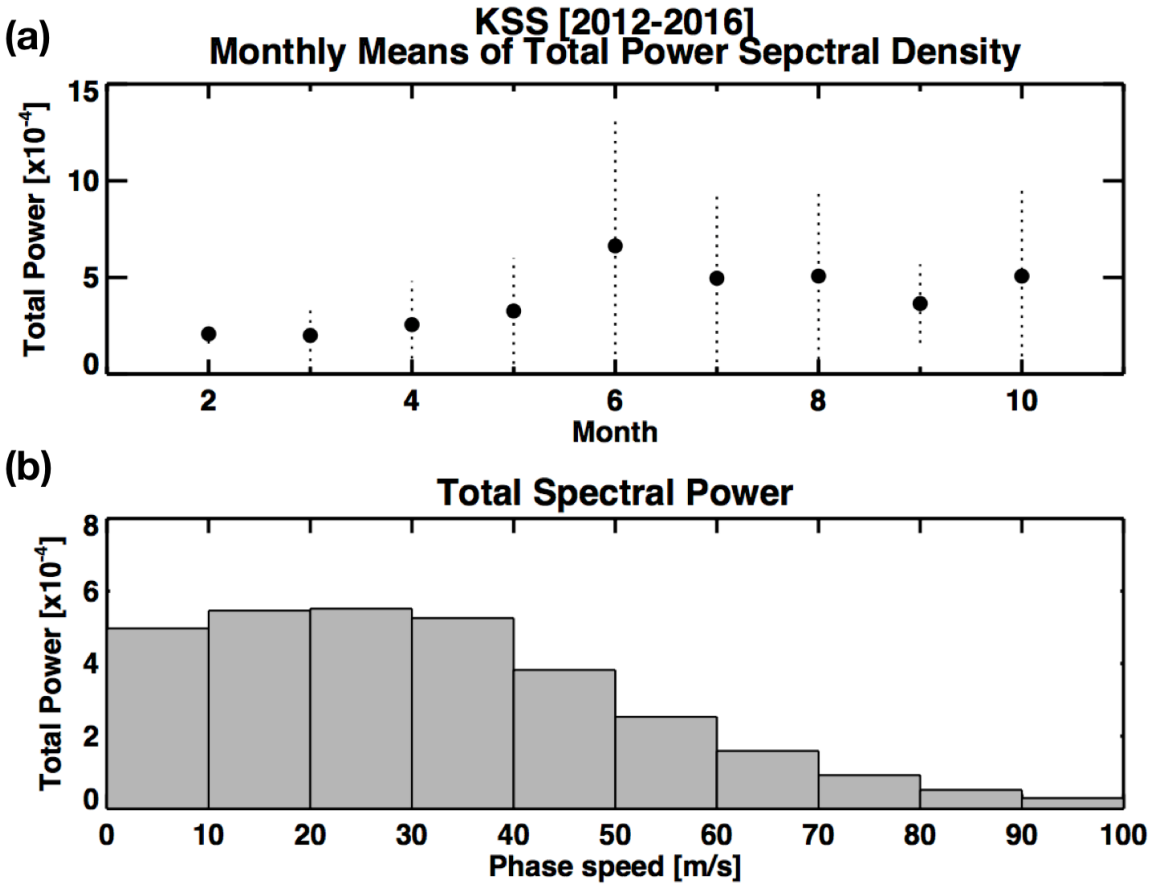

Figure 2. (a) Monthly means of total power spectral densities (black dot) and their standard deviations (dotted lines) of observed waves at KSS, and (b) histograms of total spectral powers as a function of phase speed. Note that the unit of total power is $(I'/\bar{I})^2$.

3.2 Graphical evidence of the wind filtering effect

From the five year observations we computed monthly mean PSDs as a function of propagating azimuth angles for slow, medium and fast wave groups. The results are plotted on the plane of month vs azimuth for each wave group, as shown in Figures 3a, 3b, and 3c. Also plotted are the contours of wind blocking directions. The dashed and solid contours are wind blocking directions for the lower boundaries of 10 km and 50 km, respectively. The number on the contour indicates the maximum wind speed toward that direction in the mean wind profile of that month. An upward propagating GW from the troposphere with a phase speed slower than the contour number would meet the critical layer where the phase speed is equal to the background wind and thus is expected to be blocked (either reflected downward or

absorbed) and not propagated up to the mesospheric OH airglow layer that the ASC observes. On the other hand, GWs with phase speeds faster than the contour number would not meet the critical layer, and thus are not filtered out. It is evident from Figure 3a that the slow waves are well confined by the wind blocking contours, especially dominant westward waves in winter (May-Aug) and lack of westward waves in fall (Feb and Mar) and spring (Oct). The medium speed waves are also fairly well matched with the wind blocking contours, except the southeastward waves in Oct. However, the fast waves are not confined by the wind blocking contours, especially in winter. The fast waves are not expected to be blocked because they are faster than the maximum winds in the middle atmosphere. Therefore, Figure 3a, 3b and 3c demonstrate wind blocking features in the observed mesospheric waves, providing the graphical evidence for the filtering effect.

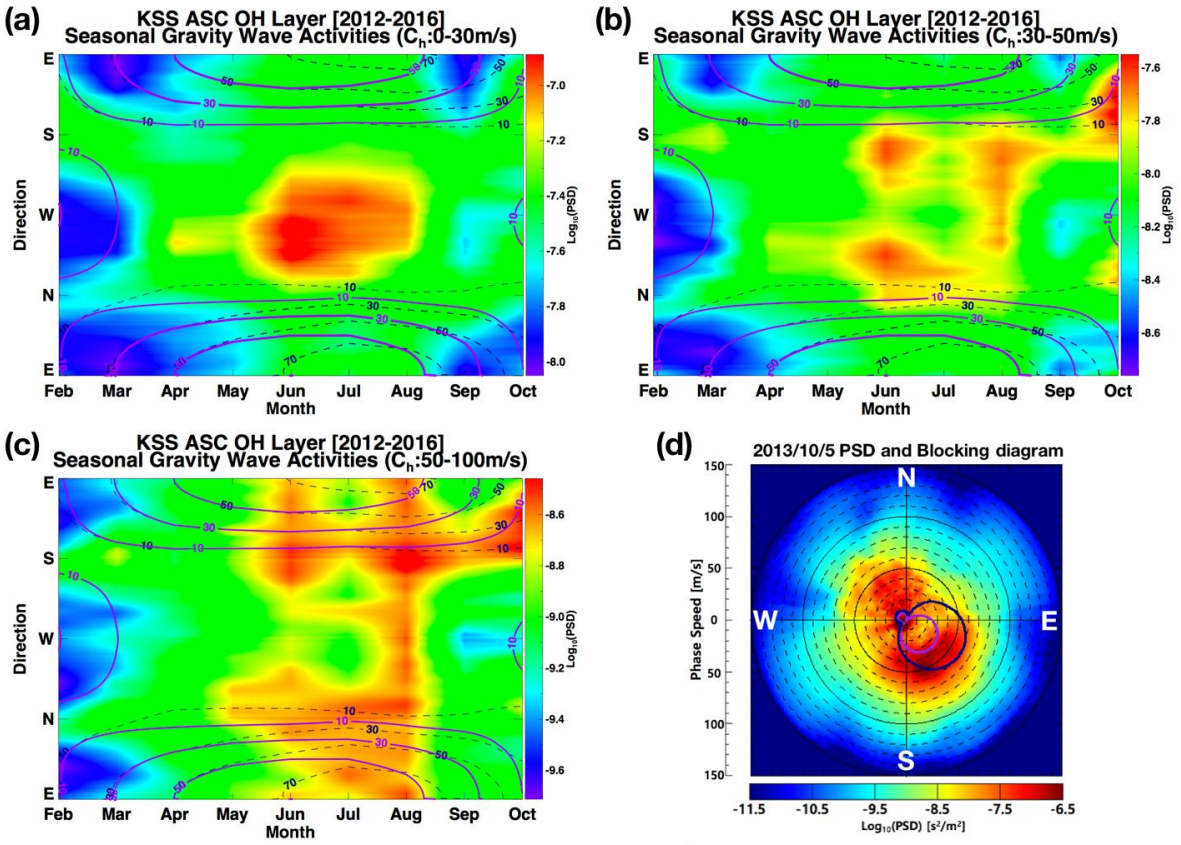

Figure 3. (a) Monthly mean power spectral densities of waves with horizontal phase speeds of 0- 30 m/s on the month – azimuth direction plane. Over-plotted are monthly mean wind blocking diagrams with the lower boundary altitudes of 50 km (purple solid contour) and of 10 km (navy dashed contour). (b) Same as in (a) except for phase speeds of 30 – 50 m/s. (c) Same as in (a) except for phase speeds faster than 50 m/s. (d) A polar plot of PSDs with wind

blocking diagrams of the 10 km (navy line) and 50 km (purple line) lower boundaries at the night of Oct. 5, 2013.

Comparison of wave directionalities from airglow images with wind blocking diagrams has been reported in previous studies (Taylor et al., 1993; Medeiros et al., 2003; Essien et al., 2018), but the diagram like Figure 3 is a new approach to demonstrate the wind filtering effect. The dominant westward mesospheric GWs have also been reported from imaging observations near KSS in the Antarctic Peninsula, such as Rothera station (67°S, 68°W) (Espy et al., 2006) and Comandante Ferraz station (62°S, 58°W) (Bageston et al., 2009). It is widely accepted that the dominance of westward propagating GWs in winter are due to wind filtering by the strong eastward stratospheric polar jet. However, the reason for propagating directions in fall and spring has not been examined in the Antarctic region.

3.3 Waves of possible mesospheric origin

Although the wind blocking diagrams explain the observed mesospheric wavs fairly well in terms of filtering effects, there are significant disparities of observed directions to the wind blocking contours. Most notable is the southeastward (SE) GWs in Oct, which invade the blocking contours. Specifically, in Figure 3a there are significant SE slow waves in Oct crossing the 30 m/s contours of the 10 km lower boundary, but not those of the 50 km lower boundary. This may mean the SE waves started above the altitude of 50 km, implying mesospheric origin. The SE waves in Oct appear also in the medium and fast speed wave groups. If the SE waves in all three groups are of the same origin, which is reasonable assumption, they are all generated in the mesosphere.

Since the wave and wind directions in the above analysis are all monthly averaged, tropospheric origin waves may occasionally propagate to the OH layer if they encountered favorable wind profiles that vary by tides or planetary waves. To examine this occasional possibility, we plotted wave PSD and blocking diagram for one example night (Oct. 5, 2013), as in Figure 3d. Over-plotted are wind blocking contours for the 10 km lower boundary (navy) and for the 50 km lower boundary (purple). There are significant SE waves inside the 10 km contour, but outside the 50

km contour. These SE waves should have been blocked by the stratospheric winds, if they are originated from the troposphere. Therefore, at least, at this particular night the observed SE waves started above 50 km, strongly suggesting mesospheric origin.

Another exception of wind blocking diagram analysis is that there are significant activities of eastward waves during winter as seen in Figure 3a and 3b. Any tropospheric eastward waves are supposed to be blocked tightly by the strong winter eastward jet in the stratosphere. Since the eastward winter jet is strong and robust, especially in June and July, the observed eastward waves in winter are likely of mesospheric origin. Furthermore, the individual power spectral diagrams, such as Figure 1b and Supporting information 1, show nearly isotropic propagating patterns in winter. Vadas et al. (2003) suggested that secondary GWs generated from body force of breaking primary waves can propagate in all directions. Recently, Becker and Vadas (2018) suggested that the secondary waves are well generated during winter from body force of breaking primary waves in the stratosphere and lower mesosphere around 60°S. Thus, the eastward wave components observed in winter may thus originate from breaking of primary waves in the stratosphere. Alternatively, they may be of tropospheric origin from distant regions, since Kogure et al. (2018) observed enhancement of GW energy over Syowa in August, and attributed them to GW refraction from various latitudes. However, Matsuda et al. (2017) compared individual PSDs with the blocking diagrams over Syowa, Halley, and McMurdo, and found the effect of wind filtering. They also noted the discrepancy between wave propagating directions and wind blocking diagrams over Davis, and speculated that it might be due to secondary GWs above the stratosphere with temporal variation. However, the SE waves in October remain unfit to the secondary wave scenario because they have predominant direction.

4 Summary and Conclusions

We analyzed all-sky OH airglow images observed at KSS for 5 years (2012-2016) using the M-transform method. The M-transform of the OH images results in magnitudes and propagating directions of short period (<1 hr) GWs. The magnitude of GWs shows clear seasonal variation, with strong activities in mid-winter. In order to understand the seasonal

304 directionality of mesospheric GWs, we constructed climatological wind blocking diagrams
305 from MERRA-2 (10-64 km) and KSS MR (80-90 km) wind data. The predominant directions
306 of observed waves with slow speeds (0-30 m/s) are clearly anti-correlated with wind blocking
307 directions, providing graphical evidence of wind filtering effects on mesospheric waves
308 observed with KSS ASC. However, we note significant eastward wave activities in winter
309 despite the strong eastward wind blocking in the middle atmosphere. The nearly isotropic
310 nature of waves during winter, including the unanticipated eastward waves, are consistent
311 with the secondary wave theory, in which the secondary waves are generated from breaking
312 of primary waves in the upper stratosphere and mesosphere. We also noted that strong south-
313 eastward GWs in spring might be generated above the altitude of ~50 km, but not fit to the
314 secondary wave theory because of their predominant directionality.

315

316 **Acknowledgments**

317 This work was supported by the grant PE20100 from the Korea Polar Research
318 Institute and studied as a part of collaboration work in ANGWIN community. M-transform
319 software was provided from National Institute of Polar Research and MERRA-2 data were
320 downloaded from following website (http://gmao.gsfc.nasa.gov/reanalysis/MERRA-2/).

321 **References**

322 Alexander, M. J., & Teitelbaum, H. (2007). Observation and analysis of a large amplitude
323 mountain wave event over the Antarctic peninsula. *Journal of Geophysical Research:*
324 *Atmosphere*, 112, D21103. http://doi.org/10.1029/2006JD008368

325 Bageston, J. V., Wrasse, C. M., Gobbi, D., Takahashi, H., & Souza, P. B. (2009). Observation
326 of mesospheric gravity waves at Comadante Ferraz Antarctica Station (62°S). *Annales*
327 *Geophysicae*, 27, 2593-2598. http://doi.org/10.5194/angeo-27-2593-2009

328 Baker, D. J., & Stair. Jr., A.T. (1988). Rocket measurements of the altitude distributions of the
329 hydroxyl airglow. *Physicaa Scripta*, 37, 611-622. http://doi.org/10.1088/0031-8949/37/4/021

330 Baumgaertner, A. J. G., & McDonald A. J. (2007). A gravity wave climatology for Antarctica
331 compiled from Challenging Minisatellite Payload/Global Positioning System (CHAMP/GPS)

radio occultations. *Journal of Geophysical Research: Atmosphere*, 112(D5), D05103. http://doi.org/10.1029/2006JD007504

Becker, E. (2012). Dynamical control of the middle atmosphere. *Space Science Reviews*, 168(1-4), 238-314. http://doi.org/10.1007/s11214-011-9841-5

Becker, E., & Vadas, S. L. (2018). Secondary gravity waves in the winter mesosphere: Results from a high-resolution global circulation model. *Journal of Geophysical Research: Atmosphere*, 123, 2605-2627. http://doi.org/10.1002/2017JD027460

de Wit, R. J., Janches, D., Fritts, D. C., Stockwell, R. G., & Coy, L. (2017). Unexpected climatological behavior of MLT gravity wave momentum flux in the lee of the Southern Andes hot spot. *Geophysical Research Letters*, 44, 1182-1191. http://doi.org/10.1002/2016GL072311

Ern, M., Preusse, P., Alexander, M. J., & Warner, C. D. (2004). Absolute values of gravity wave momentum flux derived from satellite data. *Journal of Geophysical Research: Atmosphere*, 109, D20103. http://doi.org/10.1029/2004JD004752

Espy, P. J., Hibbins, R. E., Swenson, G. R., Tang, J., Taylor, M. J., Riggin, D. M., & Fritts, D. C. (2006). Regional variations of mesospheric gravity-wave momentum flux over Antarctica. *Annales Geophysicae*, 24, 81-88. http://doi.org/10.5194/angeo-24-81-2006

Essien, P., Paulino, I., Wrasse, C. M., Campos, J. A. V., Paulino, A. R., Medeios, A. F., Buriti, R. A., Takahashi, H., Agyei-Yeboah, E., & Lins, A. N. (2018). Seasonal characteristics of small- and medium-scale gravity waves in the mesosphere and lower thermosphere over Brazilian equatorial region, *Annales Geophysicae*, 36, 899-914. http://doi.org/10.5194/angeo-36-899-2018

Fritts, D. C., & Alexander, M. J. (2003). Gravity wave dynamics and effects in the middle atmosphere. *Reviews of Geophysics*, 41(1), 1-68. http://doi.org/10.1029/2001RG000106

Gelaro, R., McCarty, W., Suárez, M. J., Todling, R., Molod, A., Takacs, L., … Zhao, B. (2017). The Modern-Era Retrospective Analysis for Reseach and Applications, version 2 (MERRA-2). *Journal of Climate*, 30(14), 5419-5454. http://doi.org/10.1175/JCLI-D-16-0759.1

Hindley, N. P., Wright, C. J., Smith, N. D., & Mitchell, N. J. (2015). The southern stratospheric gravity wave hot spot: Individual waves and their momentum fluxes measured by COSMIC GPS-RO. *Atmospheric Chemistry and Physics*, 15, 7797-7818. http://doi.org/10.5194/acp-15-7797-2015

Hoffmann, L., Xue, X., & Alexander, M. J. (2013). A global view of stratospheric gravity wave hotspots located with Atmospheric Infrared Sounder Observation. *Journal of Geophysical Research: Atmosphere*, 118, 416-434. http://doi.org/10.1029/2012JD018658

Hoffmann, L., Spang, R., Orr, A., Alexander, M. J., Holt, L. A., & Steinm O. (2017). A decadal satellite record of gravity wave activity in the lower stratosphere to study polar stratospheric cloud formation. *Atmospheric Chemistry and Physics*, 17, 2901-2920. http://doi.org/10.5194/acp-17-2901-2017

Jiang, J. H., Wu, D. L., Ekermann, S. D., & Ma, J. (2003). Mountain waves in the middle atmosphere: Microwave Limb Sounder observations and analyses. *Advanced in Space Research*, 32(5), 801-806. http://doi.org/10.1016/S0273-1177(03)00402-2

Kam, H., Jee, G., Kim, Y. H., Ham, Y. -b., & Song, I. -S. (2017). Statistical analysis of mesospheric gravity waves over King Sejong Station, Antarctica (62.2°S, 58.8°W). *Journal of Atmospheric and Solar-Terrestrial Physics*, 155, 86-94. http://doi.org/10.1016/j.jastp.2017.02.006

Kogure, M., Nakamura, T., Ejiri, M. K., Nishiyama, T., Tomikawa, Y. & Tsutsumi, M.,= (2018). Effects of horizontal wind structure on a gravity wave event in the middle atmosphere over Syowa (69°S, 40°E), the Antarctic, *Geophysical Research Letters*, 45, 5151-5157. https://doi.org/10.1029/2018GL078264

Lee, C., Kim, Y. H., Jee, G., Kim, J. -H., Won, Y. I., & Wu, D. L. (2013). Seasonal variation of wave activities near the mesopause region observed at King Sejong Station (62.22°S, 58.78°W), Antarctica. *Journal of Atmospheric and Solar-Terrestrial Physics*, 105-106, 30-38. http://doi.org/10.1016/j.jastp.2013.07.006

Lindzen, R. S. (1981). Turbulence and stress owing to gravity wave and tidal breakdown. *Journal of Geophysical Research: Oceans*, 86(C10), 9707-9714. http://doi.org/10.1029/JC086iC10p09707

Liu, X., Xu, J., Yue, J., Vadas, S. L., & Becker, E. (2019). Orographic primary and secondary gravity waves in the middle atmosphere from 16-year SABER observations. *Geophysical Research Letters*, 46, 4512-4522. http://doi.org/10.1029/2019GL082256

Matsuda, T. S., Nakamura, T., Ejiri, M. K., Tsutsumi, M., & Shiokawa, K. (2014). New statistical analysis of the horizontal phase velocity distribution of gravity waves observed by airglow imaging. *Journal of Geophysical Research: Atmosphere*, 119, 9707-9718. http://doi.org/10.1002/2014JD021543

Matsuda, T. S., Nakamura, T., Ejiri, M. K., Tsutsumi, M., Tomikawa, Y., Taylor, M. J., Zhao, Y., Pautet, P. -D., Murphy, D. J., & Moffat-Griffin, T. (2017). Characteristics of mesospheric gravity waves over Antarctica observed by Antarctic Gravity Wave Instrument Network imagers using 3-D spectral analyses. *Journal of Geophysical Research: Atmosphere*, 122, 8969-8981. http://doi.org/10.1002/2016JD026217

Medeiros, A. F., Taylor, M. J., Takahashi, H., Batista, P. P., & Gobbi, D. (2003). An investigation of gravity wave activity in the low-latitude upper mesosphere: Propagation direction and wind filtering, *Journal of Geophysical Research: Atmosphere*, 108(D14), 4411, http://doi.org/2002JD002593

Park, J., Lühr, H., Lee, C., Kim, Y. H., Jee, G., & Kim, J. -H. (2014). A climatology of medium-scale gravity wave activity in the midlatitude/low-latitude daytime upper thermosphere as observed by CHAMP. *Journal of Geophysical Research: Space Physics*, 119, 2187-2196. http://doi.org/10.1002/2013JA019705

Perwitasari, S., Nakamura, T., Kogure, M., Tomikawa, Y., Ejiri, M. K., & Shiokawa, K. (2018). Comparison of gravity wave propagation directions observed by mesospheric airglow imaging at three different latitudes using the M-transform. *Annales Geophysicae,* 36(6), 1597-1605. http://doi.org/10.5194/angeo-36-1597-2018

Preusse, P., Dörnbrack, A., Eckermann, S. D., Riese, M., Schaeler, B., Bacmeister, J. T., Broutman, D., & Crossmann, K. U. (2002), Space-based measurements of stratospheric mountain waves by CRISTA, 1. Sensitivity, analysis method, and a case study. *Journal of Geophysical Research: Atmosphere*, 107(D23), 8178. http://doi.org/10.1029/2001JD000699

Sato, K., Watanabe, S., Kawatani, Y., Tomikawa, Y., Miyazaki, K., & Takahashi, M. (2009). On the origin of mesospheric gravity waves. *Geophysical Research Letters*, 36, L19801. http://doi.org/10.1029/2009GL039908

Sato, K., Tateno, S., Watanabe, S., & Kawatani, Y. (2012). Gravity wave characteristics in the Southern hemisphere revealed by a high-resolution Middle-atmosphere general circulation model. *Journal of the Atmospheric Sciences*, 65(4), 1378-1396. http://doi.org/10.1175/JAS-D-11-0101.1

Taylor, M. J., Ryan, E. H., Tuan, T. F., & Edwards, R. (1993). Evidence of preferential directions for gravity wave propagation due to wind filtering in the middle atmosphere. *Journal of Geophysical Research: Atmosphere*, 98, 6047-6057. http://doi.org/10.1029/92JA02604.

Vadas, S. L., Fritts, D. C., & Alexander, M. J. (2003). Mechanism for the generation of secondary waves in wave breaking regions. *Journal of the Atmospheric Sciences*, 60(1), 194-214. http://doi.org/10.1175/1520-0469(2003)060<0194:MFTGOS>2.0.CO;2.